https://doi.org/10.5194/egusphere-2026-3934
Preprint. Discussion started: 11 August 2026

Accelerated Warming Shifts the Balance Between Thermodynamic Moistening and ENSO-related Variability in Atmospheric Water Vapour

Yu Gao[1], Wenyuan Zhang[1,2], Shubi Zhang[1], Zhiping Chen[3], Chao Liu[4], and Long Li[5]

[1]School of Environment and Spatial Informatics, China University of Mining and Technology, Jiangsu, China
[2]Institute of Geodesy and Photogrammetry, ETH Zurich, Zurich, Switzerland
[3]School of Surveying and Geoinformation Engineering, East China University of Technology, Nanchang, China
[4]School of Geomatics, Anhui University of Science and Technology, Huainan, China
[5]YUEKUANGLIANHAI(Guangdong) Intelligent Technology Co., Ltd, Guangdong, China

Correspondence: Wenyuan Zhang (zhangwy@cumt.edu.cn)

Abstract. Atmospheric water vapour is shaped by both sustained global warming (GW) and El Niño–Southern Oscillation (ENSO), but how these two climate influences are expressed in the water-vapour field and how their coupling changes under accelerated warming remain poorly quantified. Here we comprehensively characterize the links between global GNSS-derived precipitable water vapour (PWV), a vertically integrated measure of atmospheric moisture, and both GW and ENSO by integrating Independent Component Analysis (ICA) and Convergent Cross Mapping (CCM). Warming-related and ENSO-related PWV signals are extracted from the GNSS PWV field using ICA and are denoted as PWV_{GW} and PWV_{ENSO}, respectively. PWV_{GW} is closely associated with GW ($r = 0.79$), and CCM supports dominant $GW \rightarrow PWV_{GW}$ coupling. By contrast, PWV_{ENSO} responds to ENSO with an approximately 12-month lag ($r = 0.77$), and extended CCM indicates bidirectional coupling between ENSO and PWV_{ENSO}. After the transition to accelerated warming around 2013, the sensitivity of PWV_{GW} to temperature increases markedly, consistent with enhanced thermodynamic moistening. At the same time, the $ENSO \rightarrow PWV_{ENSO}$ coupling weakens despite stronger ENSO variability. These findings suggest that accelerated warming shifts the balance between long-term thermodynamic moistening and interannual ENSO-related variability in the atmospheric water vapour field.

1 Introduction

El Niño–Southern Oscillation (ENSO), the dominant mode of interannual climate variability, reorganizes tropical convection and large-scale atmospheric circulation, thereby modulating moisture transport and producing widespread variations in atmospheric water vapour (Curtis, 2008; Li et al., 2021). On longer timescales, global warming imposes a thermodynamic constraint on atmospheric moisture. According to the Clausius–Clapeyron relation, the moisture-holding capacity of the atmosphere increases by approximately 7% per kelvin of warming, linking temperature rise to increases in atmospheric water vapour through a well-established physical mechanism (Martínková and Kyselý, 2020; Ali et al., 2021; Nayak and Takemi, 2025). Because water vapour is the most abundant greenhouse gas and plays a central role in the global energy and water cycles (Sherwood

https://doi.org/10.5194/egusphere-2026-3934
Preprint. Discussion started: 11 August 2026

et al., 2010; Wang et al., 2018; Patel and Kuttippurath, 2023; Edström and Dahlbäck, 2024), separating ENSO-related dynamical variability from warming-related thermodynamic moistening is essential for understanding how the atmospheric branch of the hydrological cycle responds to a changing climate. However, the relative contributions of these two processes to observed global land water-vapour variability, and the extent to which their coupling changes under accelerated warming, remain insufficiently constrained.

Ground-based Global Navigation Satellite System (GNSS) networks provide continuous, all-weather observations of precipitable water vapour (PWV), a measure of vertically integrated atmospheric water vapour (Yuan et al., 1993; Rocken et al., 1993; Nilsson and Elgered, 2008; Jin et al., 2008; Zhang et al., 2024; Kelsey et al., 2022). GNSS-derived PWV is obtained from signal propagation delays and has become an important independent source of atmospheric moisture information (Bevis et al., 1992, 1994; Rocken et al., 1995; Tregoning et al., 1998; Basili et al., 2001; He et al., 2020). The long-term stability, high temporal resolution, and broad spatial coverage of GNSS records make them particularly suitable for investigating climate-scale variations in land atmospheric moisture (Zhang et al., 2015). Nevertheless, identifying specific large-scale climate signals from GNSS PWV remains challenging because the observed time series contain a mixture of long-term trends, seasonal variations, interannual variability, regional circulation effects, and local hydrometeorological noise.

Previous studies have used decomposition and covariance-based methods, including Empirical Orthogonal Functions (EOF) (Lu et al., 2020), Singular Spectrum Analysis (SSA) (Zhang et al., 2015; Baldysz et al., 2021; Wang and Ren, 2025), Multivariate Singular Spectrum Analysis (MSSA) (Zhao et al., 2020), and Maximum Covariance Analysis (MCA) (Ding and Fu, 2018), to investigate climate-related signals in GNSS-derived PWV. These methods have provided useful evidence for ENSO-related water-vapour variability, but they generally emphasize linear covariance structures, orthogonality, or variance maximization. Such assumptions may be restrictive when different climate signals are statistically mixed, non-Gaussian, or not organized according to maximum variance (Jutten and Herault, 1991; Aires et al., 2000). As a result, ENSO-related PWV signals may be partially mixed with other modes of variability, leading to weak or ambiguous interpretations of the ENSO imprint in the atmospheric water-vapour field (Wang et al., 2018; Zhao et al., 2020). Moreover, most previous analyses have relied mainly on correlation or regression, which can quantify statistical association but provide limited information on the direction and strength of dynamical coupling. It therefore remains unclear whether ENSO primarily acts as an external driver of PWV variability, whether water vapour feeds back onto ENSO-related dynamics, or whether the strength of this coupling has changed as the climate system has warmed.

A further unresolved issue is how accelerated warming modifies the relationship between long-term thermodynamic moistening and interannual ENSO-related variability. Recent increases in global temperature indicate that the climate system has entered a period of more rapid warming (Shu et al., 2024; Bevacqua et al., 2024; Gebrechorkos et al., 2025; Fischer et al., 2025; Foster and Rahmstorf, 2026). Under such conditions, the background thermodynamic control on atmospheric moisture may strengthen, potentially altering the sensitivity of PWV to temperature and changing the apparent influence of ENSO on water-vapour variability. However, observational evidence for such a shift remains limited, especially from long-term, globally distributed ground-based PWV records.

https://doi.org/10.5194/egusphere-2026-3934
Preprint. Discussion started: 11 August 2026

Here, we analyse monthly PWV from 627 globally distributed GNSS stations from January 2003 to December 2025. We use Independent Component Analysis (ICA) to separate statistically independent PWV components associated with global warming and ENSO, hereafter denoted as PWV_{GW} and PWV_{ENSO}. The temporal evolution of these components is compared with standard climate indices to characterize the corresponding lead–lag relationships, while their spatial fingerprints are examined to identify the geographic patterns of PWV responses associated with global warming and ENSO. To move beyond correlation-based interpretation, we apply Convergent Cross Mapping (CCM) to evaluate the direction and strength of coupling between each climate index and its associated PWV component. We further use the Bayesian Estimator of Abrupt Change, Seasonal Change, and Trend (BEAST) to identify a structural breakpoint in global mean temperature and to examine whether the PWV–climate coupling differs between the earlier and accelerated warming periods. Finally, changes in thermodynamic PWV sensitivity and ENSO variability are quantified to interpret the coupling results in a physical context.

This study aims to answer three questions: (1) Can warming-related and ENSO-related signals be separated from the global GNSS-observed land PWV field? (2) What are the lead–lag relationships and the direction and strength of coupling between these PWV components and their associated climate forcings and modes? (3) Has accelerated warming altered the balance between long-term thermodynamic moistening and interannual ENSO-related water-vapour variability? By addressing these questions, we provide observational evidence for how global land atmospheric water vapour responds jointly to sustained warming and ENSO-related climate variability.

2 Data and Methods

2.1 Global GNSS PWV Dataset

Monthly PWV records were obtained from the global GNSS PWV dataset archived at PANGAEA (https://doi.pangaea.de/10.1594/PANGAEA.982476) (Wang et al., 2025), which covers the period from November 2001 to December 2021. This dataset provides station-level PWV estimates derived from GNSS tropospheric delay products using a unified processing strategy and standardized quality-control procedures. To ensure that the selected records were suitable for climate-scale variability analysis, we applied strict station-selection criteria. First, daily PWV was calculated as the mean of all available hourly values only for days with at least six valid hourly observations; otherwise, the daily value was treated as missing. Second, stations with a daily missing-data rate greater than 20% over the available record were excluded to preserve temporal continuity and to reduce the influence of long data gaps on subsequent decomposition analyses. After applying these criteria, 627 stations distributed across the mainland regions were retained (Fig. 1).

Because the PANGAEA dataset ends in December 2021, the selected station records were extended to December 2025 using GNSS tropospheric products from the Nevada Geodetic Laboratory (NGL, https://geodesy.unr.edu/), where available for the retained stations. The PANGAEA and NGL records are based on the same physical quantity, namely GNSS-derived atmospheric delay converted to PWV, but potential inconsistencies between the two products were minimized by applying the same temporal aggregation and quality-control procedures before merging. Daily PWV values were aggregated into monthly means, and a monthly value was retained only when at least 10 valid daily values were available. This threshold was used to

https://doi.org/10.5194/egusphere-2026-3934
Preprint. Discussion started: 11 August 2026

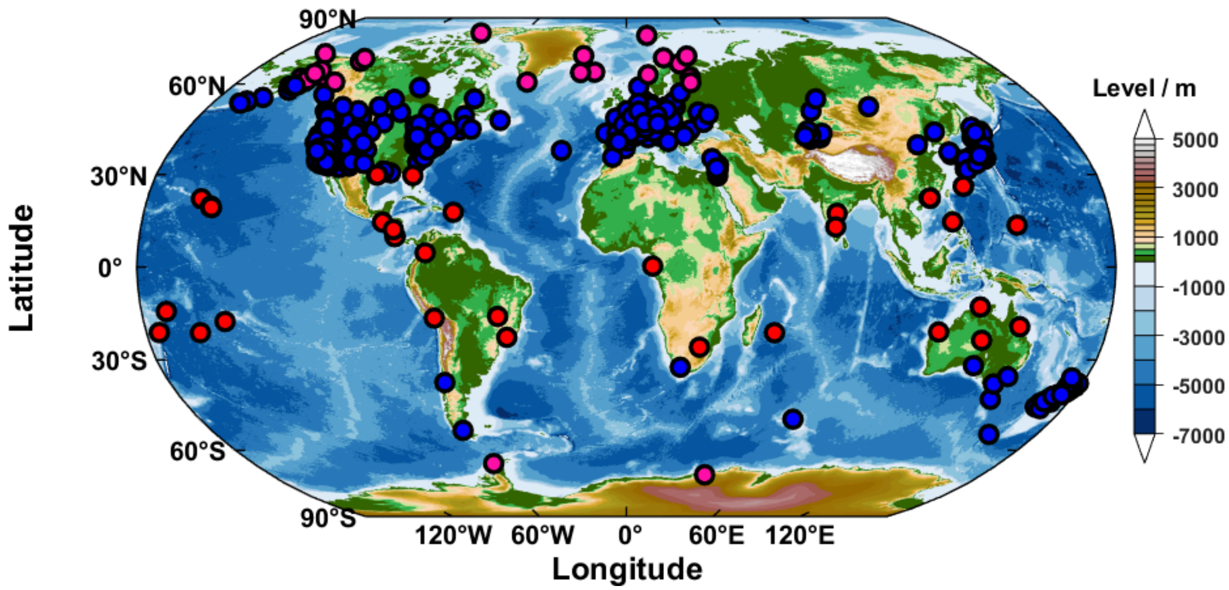

Figure 1. Global distribution of 627 GNSS stations by latitude band.

limit sampling-related biases in monthly means while retaining sufficient temporal coverage. The PANGAEA and NGL records were then combined to form a continuous monthly PWV dataset covering January 2003 to December 2025, with 276 monthly time steps.

Remaining gaps in the monthly series were filled using an iterative SSA method (Yi and Sneeuw, 2021), which estimates missing values from the dominant temporal structures of each station time series while preserving the observed values. This step was applied only after the monthly aggregation and station screening procedures, because ICA and CCM require temporally continuous input series and can be sensitive to artificial discontinuities.

The monthly global mean surface temperature anomaly was obtained from the GISTEMP v4 dataset (Lenssen et al., 2024), and the Oceanic Niño Index (ONI) was obtained from the NOAA Climate Prediction Center (https://www.cpc.ncep.noaa.gov/). Both climate indices were used at monthly resolution to match the temporal resolution of the GNSS PWV records.

2.2 Independent Component Analysis

To separate climate-related signals embedded in the global GNSS PWV field, we applied ICA to the monthly PWV anomaly matrix constructed from 627 GNSS stations and 276 monthly time steps from January 2003 to December 2025. PWV is influenced by multiple processes operating on different timescales, such as long-term thermodynamic moistening, ENSO-related circulation changes, and regional moisture transport. Previous studies have shown that ENSO-related PWV variability can exhibit nonlinear temporal behaviour, making simple linear covariance-based decomposition insufficient for fully isolating ENSO-related water-vapour variability (Wang et al., 2018; Zhao et al., 2020; Aires et al., 2000). ICA decomposes the observed

https://doi.org/10.5194/egusphere-2026-3934
Preprint. Discussion started: 11 August 2026

data into statistically independent source signals (Comon, 1994; Hyvärinen and Oja, 2000). This makes ICA suitable for separating mixed climate influences in GNSS PWV records. Unlike EOF analysis, which identifies orthogonal modes that maximize explained variance, ICA seeks statistically independent components by minimizing mutual information. ICA is therefore used here to isolate physically interpretable PWV components rather than to rank modes by variance contribution.

Before ICA, the monthly PWV records were preprocessed in three steps. First, the seasonal cycle at each station was removed by subtracting the long-term mean for each calendar month (Sun and Lan, 2021). Second, the deseasonalized anomalies were smoothed using a three-point 1-2-1 binomial filter to reduce month-to-month noise (Wang et al., 2012). Third, a low-pass filter was applied to suppress high-frequency fluctuations and emphasize large-scale climate variability (Chen et al., 2018, 2024). Following Chen et al. (2024), different cut-off frequencies were tested, and the final cut-off frequency was set to 8.5 because it provided the clearest separation of the warming- and ENSO-related PWV components.

Mathematically, ICA decomposes the preprocessed PWV anomaly matrix $\mathbf{X} \in \mathbb{R}^{M \times T}$, where $M = 627$ and $T = 276$, into spatial loadings and independent temporal components:

$$\mathbf{X} = \mathbf{AS} \tag{1}$$

where $\mathbf{A} \in \mathbb{R}^{M \times P}$ contains the spatial loading of each component, and $\mathbf{S} \in \mathbb{R}^{P \times T}$ contains the corresponding independent temporal components. The FastICA algorithm was used to estimate the independent components (Bingham and Hyvärinen, 2000; Chen et al., 2024). The number of retained components was set to $P = 6$, allowing the dominant large-scale PWV signals to be separated while avoiding excessive fragmentation of physically interpretable modes.

Components associated with ENSO and global warming were identified using their peak lagged correlations with ONI and GMST, respectively, together with the physical consistency of their spatial loadings. These components are denoted as PWV_{ENSO} and PWV_{GW}. Because the sign of each ICA component is arbitrary, the sign of each selected component was adjusted so that positive temporal amplitudes correspond to the positive phase of the associated climate index at the identified peak lag. The spatial loading then indicates whether PWV increases or decreases during that phase. This sign convention is used only for phase interpretation, while directional coupling is assessed separately using CCM.

2.3 Global GNSS PWV Dataset

To investigate nonlinear causal interactions between climate variability and atmospheric water vapour, CCM was employed to quantify the directional coupling between the climate indices (GW, $ENSO$) and the extracted PWV components (PWV_{GW} and PWV_{ENSO}) (Sugihara et al., 2012). CCM is based on state-space reconstruction theory and provides a data-driven framework for detecting causality in nonlinear dynamical systems (Takens, 1981). Unlike conventional correlation analysis, CCM determines whether information about one variable is embedded in the reconstructed state-space manifold of another variable, thereby distinguishing causal interactions from simple statistical associations.

https://doi.org/10.5194/egusphere-2026-3934
Preprint. Discussion started: 11 August 2026

2.3.1 State-Space Reconstruction

According to Takens' embedding theorem (Takens, 1981), the dynamics of a nonlinear system can be reconstructed from a single observed variable through time-delay embedding. For a given time series $Y(t)$, the shadow manifold M_Y is reconstructed as

$$M_Y(t) = [Y(t), Y(t-\tau), \ldots, Y(t-(E-1)\tau)], \tag{2}$$

where E denotes the embedding dimension and τ is the time delay. The embedding dimension determines the number of reconstructed coordinates used to represent the system dynamics, while τ controls the temporal spacing between adjacent coordinates.

To ensure the fidelity of phase-space reconstruction, the embedding parameters (E and τ) were optimized independently for each variable pair and study period. Specifically, the embedding dimension E was determined using the False Nearest Neighbors (FNN) algorithm (Kennel et al., 1992), and the smallest value corresponding to either an FNN percentage below 5% or the global minimum was selected. The optimal time delay τ was estimated from the first local minimum of the Average Mutual Information (AMI) function (Fraser and Swinney, 1986). This combined approach ensures that the reconstructed coordinates are sufficiently independent to capture the underlying system dynamics while minimizing redundant information.

If variable X causally influences variable Y, then information associated with X is expected to be encoded within the reconstructed manifold M_Y (Sugihara et al., 2012; Ban et al., 2025). Consequently, the historical states of X can be estimated from the neighboring trajectories on M_Y.

2.3.2 Cross Mapping and Convergence

For each target point on the reconstructed manifold M_Y, the $E+1$ nearest neighbors are identified according to Euclidean distance:

$$d_i = \|M_Y(t) - M_Y(t_i)\|, \tag{3}$$

where d_i represents the distance between the target point and its neighboring states. The corresponding values of X associated with these neighboring states are then used to estimate $\hat{X}(t)$ through weighted averaging:

$$\hat{X}(t) = \sum_{i=1}^{E+1} w_i X(t_i), \tag{4}$$

where the weights are calculated as

$$w_i = \frac{\exp(-d_i/d_1)}{\sum_{j=1}^{E+1} \exp(-d_j/d_1)}, \tag{5}$$

and d_1 is the minimum neighbor distance used for normalization.

https://doi.org/10.5194/egusphere-2026-3934
Preprint. Discussion started: 11 August 2026

The cross-map skill is quantified using the Pearson correlation coefficient between the reconstructed series $\hat{X}(t)$ and the observed series $X(t)$:

$$\rho = \mathrm{corr}\left(X(t), \hat{X}(t)\right). \tag{6}$$

A causal relationship is inferred when the cross-map skill increases and gradually converges with increasing library size L Bonotto et al. (2022); Ban et al. (2025). In this context, convergence indicates that the reconstructed manifold contains stable dynamical information about the causal variable rather than random statistical similarity.

2.3.3 Significance Testing

To evaluate the robustness of the inferred causal relationships, statistical significance was assessed using 1,000 phase-randomized surrogate series (Theiler et al., 1992; Ebisuzaki, 1997). Each surrogate was generated by randomizing the Fourier phases while preserving the amplitude spectrum, thereby retaining the original power spectrum and autocorrelation structure while removing deterministic coupling between variables. CCM analysis was repeated for all surrogate realizations, and the significance level was estimated by comparing the observed cross-map skill with the surrogate distribution. The p value was defined as the fraction of surrogate ρ values exceeding the observed ρ. Causal relationships were considered statistically significant when $p < 0.05$.

2.4 Extended Convergent Cross Mapping

Standard CCM can identify whether two variables are dynamically coupled through state-space reconstruction (Sugihara et al., 2012). However, Ye et al. (2015) pointed out that standard CCM may not reliably distinguish true bidirectional causality from generalized synchrony induced by strong unidirectional forcing. In strongly coupled systems, significant cross-map skills may appear in both directions because the response variable becomes synchronized with the driver. Therefore, standard CCM alone may not fully resolve the temporal direction of causality.

To address this limitation, we further applied the extended CCM framework proposed by Ye et al. (2015), which evaluates the lag-dependent cross-map skill between variables. Specifically, the reconstructed manifold of one variable is used to estimate the temporally shifted state of the other variable:

$$X(t) \rightarrow Y(t+\delta), \tag{7}$$

where δ denotes the temporal offset between the two variables. By systematically varying δ, the temporal structure of the causal interaction can be examined.

Following Ye et al. (2015), the lag corresponding to the maximum cross-map skill is defined as the optimal lag:

$$\delta_{\mathrm{opt}} = \arg\max_{\delta} \rho(\delta). \tag{8}$$

The sign of the optimal lag δ_{opt} provides a diagnostic criterion for distinguishing true delayed causality from generalized synchrony. For a true causal relationship in which X drives Y, the maximum cross-map skill is expected to occur at a negative

https://doi.org/10.5194/egusphere-2026-3934
Preprint. Discussion started: 11 August 2026

optimal lag ($\delta_{\mathrm{opt}} < 0$), indicating that the present state of the response variable Y contains information about the past state of the driver X. In contrast, positive optimal lags are more consistent with generalized synchrony or delayed synchronization due to strong forcing rather than with genuine bidirectional coupling.

The statistical significance of the lag-dependent CCM results was evaluated using the same phase-randomized surrogate approach described in the previous subsection. Results were considered statistically significant when $p < 0.05$. Because both GW and PWV_{GW} are strongly influenced by long-term monotonic trends and exhibit pronounced nonstationary characteristics, additional preprocessing was required prior to CCM analysis. For the full-period CCM and extended CCM analyses, the long-term trends were removed to reduce the influence of shared low-frequency variability and to avoid inflated cross-map skill arising from common trends.

To further investigate how the coupling evolves under different warming conditions, the full record was subsequently divided into shorter subperiods. However, CCM analysis is no longer suitable for the segmented GW and PWV_{GW} series. The shorter records substantially reduce the available low-frequency variability, and detrending further weakens the remaining dynamical structure, particularly during the weak-warming phase, where the residual signals become easily dominated by noise. Under these conditions, the reconstructed manifolds no longer contain sufficient nonlinear information to support reliable CCM inference. Therefore, instead of segmented CCM analysis, linear regression was applied to the original subperiod series to quantify the sensitivity of PWV_{GW} to temperature changes under different warming regimes.

2.5 BEAST Breakpoint Detection and Subperiod Analysis

To detect structural changes in the global warming rate, we applied the BEAST algorithm to the global mean temperature series (Zhao et al., 2019). BEAST decomposes a time series into seasonal, trend, and noise components within a Bayesian framework while simultaneously identifying potential changepoints. In this study, we focused on the trend component $T(t)$, which represents the long-term evolution of global mean temperature.

The trend was modeled as a piecewise polynomial. For a model with k changepoints located at $\tau_1, \tau_2, \ldots, \tau_k$, the trend can be expressed as

$$T(t) = \sum_{j=0}^{k} \beta_j(t)\, I\big(t \in [\tau_j, \tau_{j+1})\big), \tag{9}$$

where $I(\cdot)$ is an indicator function and $\beta_j(t)$ is a polynomial of order p (here $p = 1$, i.e., piecewise linear) within each segment. Rather than solving for a single best set of changepoints, BEAST treats both the number k and the locations τ as random variables and samples their posterior distribution via Markov Chain Monte Carlo. The final trend estimate is obtained by averaging over all sampled models:

$$\hat{T}(t) \approx \frac{1}{N} \sum_{i=1}^{N} T(t, M_i), \tag{10}$$

https://doi.org/10.5194/egusphere-2026-3934
Preprint. Discussion started: 11 August 2026

where M_i denotes the ith sampled model in the posterior ensemble and N is the total number of sampled models. This averaging process yields a posterior changepoint probability at each time step, where a sharp peak in the posterior probability distribution $P(\tau \mid y)$ indicates a robust structural break.

Applied to the global mean temperature series, BEAST identifies the most probable breakpoint at October 2013 (posterior probability = 0.81), separating a slow-warming phase (P1) from an accelerated-warming phase (P2). Based on this division, the PWV components (PWV_{GW} and PWV_{ENSO}) and climate indices were segmented accordingly. Within each subperiod, we repeat both the lagged-correlation and CCM analyses to determine whether coupling strength and directionality shift between these warming phases.

3 Result

3.1 Separated warming and ENSO signals in global GNSS PWV

The ICA-derived warming-related component (PWV_{GW}) exhibits a clear long-term increase over the study period (Fig. 2c), closely following the rise in global mean temperature. The lag-correlation analysis shows a peak correlation of $r = 0.79$ at zero lag, indicating a nearly synchronous relationship between PWV_{GW} and global mean temperature. This synchronous behaviour is consistent with a thermodynamic control on atmospheric moisture, as expected from the Clausius–Clapeyron relationship. The spatial loading pattern of PWV_{GW} provides further support for this interpretation (Fig. 2a). Because the temporal evolution of PWV_{GW} is positively correlated with global mean temperature, the predominantly positive loadings indicate that GNSS-observed land PWV generally increases during the positive phase of the warming-related component. The predominantly positive and spatially coherent loading pattern suggests that PWV_{GW} captures a large-scale warming-related moistening signal in the global land PWV field.

Unlike PWV_{GW}, PWV_{ENSO} is dominated by interannual variability rather than a long-term trend (Fig. 2d). Its fluctuations closely follow those of the ONI, with a peak correlation of $r = 0.77$ reached when ONI leads PWV_{ENSO} by 12 months. This lagged relationship indicates that ENSO-related SST variability is followed by a delayed adjustment in the GNSS-observed PWV field. The spatial loading pattern of PWV_{ENSO} differs markedly from that of PWV_{GW} (Fig. 2b). Significant loading values are predominantly found in tropical regions, where the water vapour response to sea surface temperature (SST) anomalies is most direct and pronounced. This behavior is physically consistent with the large-scale influence of ENSO on tropical SST and atmospheric circulation (Diaz et al., 2001). Through these coupled ocean-atmosphere variations, ENSO can substantially affect the distribution and variability of atmospheric moisture, leading to pronounced PWV anomalies in the tropics. Thus, PWV_{ENSO} represents an interannual water-vapour signal linked to ENSO-related dynamical variability rather than to the long-term thermodynamic moistening captured by PWV_{GW}.

Together, these results indicate that warming-related thermodynamic moistening and ENSO-related interannual variability are expressed as distinct components in the global GNSS PWV record, providing a basis for the coupling analyses below.

https://doi.org/10.5194/egusphere-2026-3934
Preprint. Discussion started: 11 August 2026

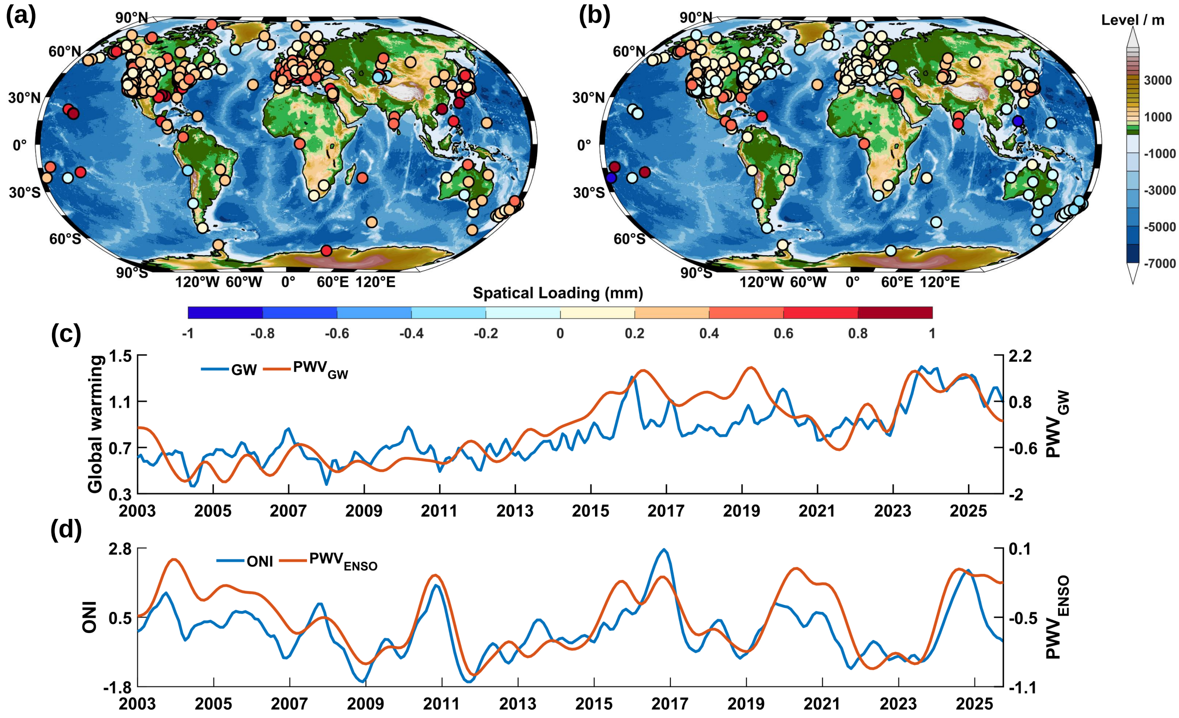

Figure 2. Spatial patterns and temporal evolution of the ICA-derived PWV modes associated with global warming and ENSO. (a)–(b) Spatial loading patterns of PWV_{GW} and PWV_{ENSO}. (c)–(d) Temporal evolution of PWV_{GW} with global warming (GW) and PWV_{ENSO} with the ONI, respectively. For visual comparison, the ONI series in (d) is shifted forward by 12 months, corresponding to the lag at which ONI leads PWV_{ENSO}.

3.2 Directional coupling between climate variability and PWV components

To investigate the directional interactions between the extracted PWV components and the corresponding climate indices, CCM analysis was performed for the full 2003–2025 period. In CCM, causal influence is inferred from the convergence of the cross-map skill (ρ) with increasing library size together with statistical significance, rather than from the absolute magnitude of ρ. As shown in Fig. 3 and Fig. 4, the warming and ENSO modes exhibit markedly different causal behaviors.

For the warming-related mode, both directions exhibit convergence as the library size increases (Fig. 3a). Here, the notation $X \rightarrow Y$ denotes cross mapping from the reconstructed manifold of Y to estimate the states of X, which is interpreted as the causal influence of X on Y. The cross-map skill for $GW \rightarrow PWV_{GW}$ converges to $\rho = 0.84$ and passes the 95% significance test based on phase-randomized surrogates ($p = 0.001$; Fig. 3b). In contrast, although the reverse direction $PWV_{GW} \rightarrow GW$ also shows convergence with a cross-map skill of $\rho = 0.55$, it does not reach the 95% significance level ($p = 0.135$; Fig. 3c). These results indicate a significant causal influence of global warming on PWV_{GW}. These results indicate a significant causal influence of global warming on PWV_{GW}, whereas the reverse direction is not statistically robust within the CCM framework.

https://doi.org/10.5194/egusphere-2026-3934
Preprint. Discussion started: 11 August 2026

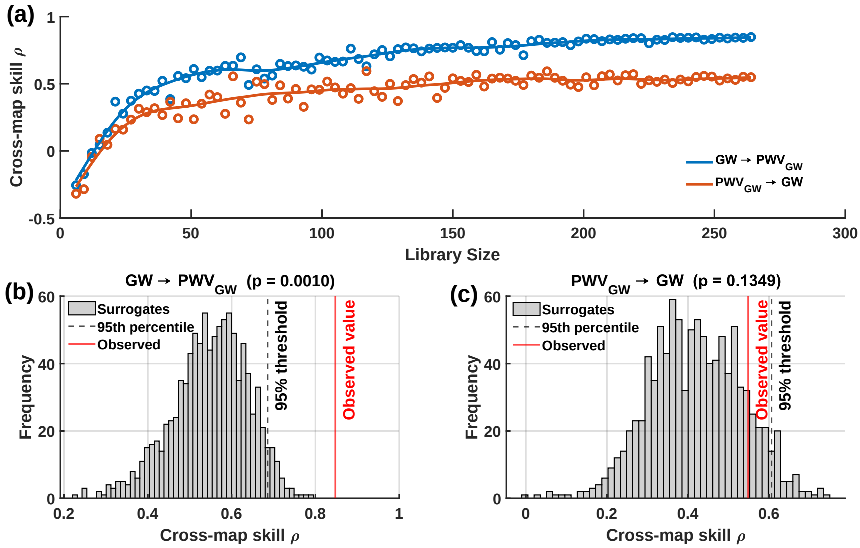

Figure 3. CCM analysis between GW and PWV_{GW}. (a) Convergence of cross-map skill (ρ) with increasing library size for both directions. (b)–(c) Phase-randomized surrogate significance tests for $GW \rightarrow PWV_{GW}$ and $PWV_{GW} \rightarrow GW$, respectively. The red line denotes the observed cross-map skill, and the dashed line indicates the 95% surrogate threshold.

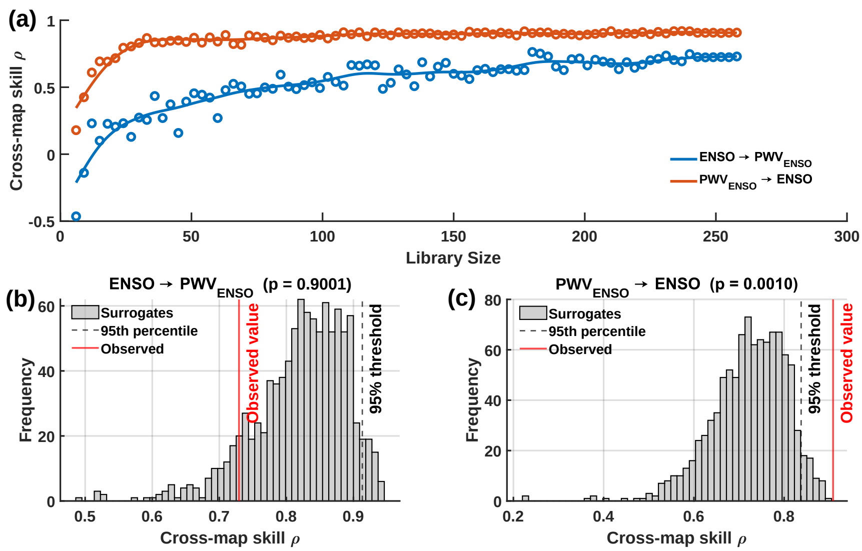

Figure 4. CCM analysis between ENSO and PWV_{ENSO}. (a) Convergence of cross-map skill (ρ) with increasing library size for both directions. (b)–(c) Phase-randomized surrogate significance tests for $ENSO \rightarrow PWV_{ENSO}$ and $PWV_{ENSO} \rightarrow ENSO$, respectively. The red line denotes the observed cross-map skill, and the dashed line indicates the 95% surrogate threshold.

https://doi.org/10.5194/egusphere-2026-3934
Preprint. Discussion started: 11 August 2026

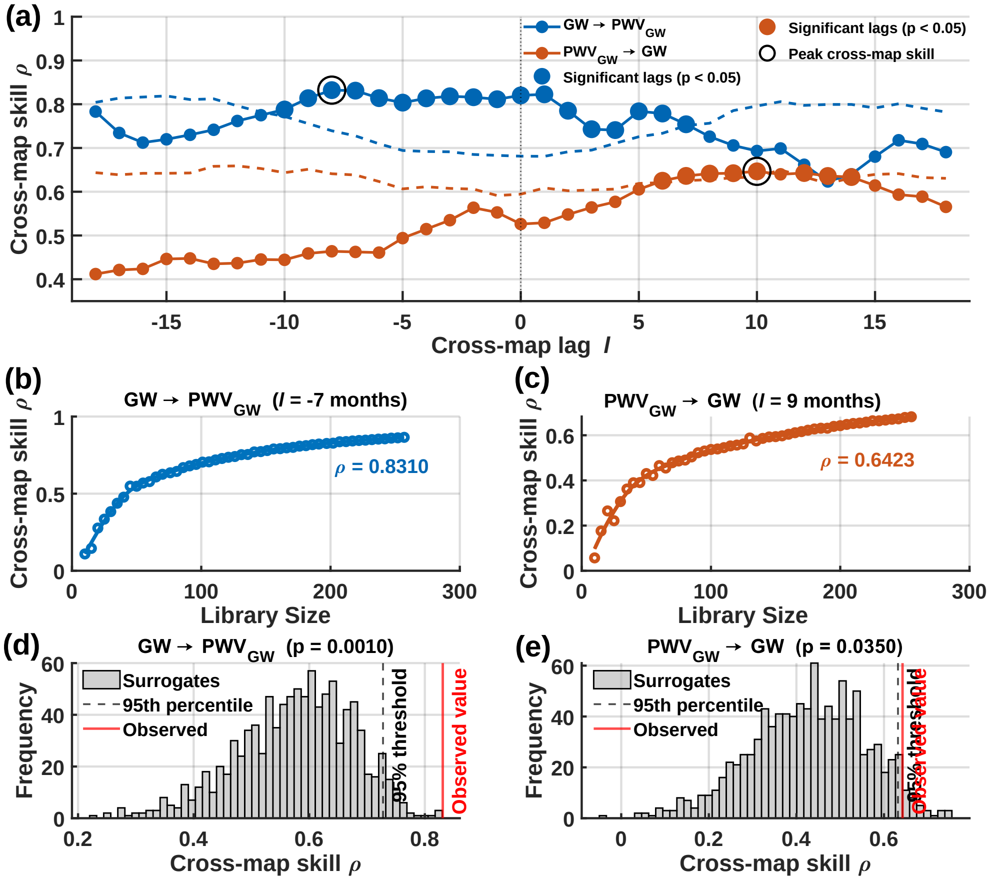

Figure 5. Extended CCM analysis between GW and PWV_{GW}. (a) Lag-dependent cross-map skill (ρ) for both directions over lags from -18 to $+18$ months. Large filled circles indicate lags passing the 95% surrogate significance test, black circles denote the optimal lag with maximum cross-map skill, and dashed lines represent the corresponding 95% surrogate thresholds. (b)–(c) Convergence of cross-map skill with increasing library size at the optimal lag for $GW \rightarrow PWV_{GW}$ and $PWV_{GW} \rightarrow GW$, respectively. (d)–(e) Phase-randomized surrogate significance tests at the optimal lag for each direction.

This asymmetric relationship is consistent with the thermodynamic dependence of atmospheric moisture on temperature and agrees with the established water vapour–radiation feedback mechanism (Schneider et al., 1999; Yang and Tan, 2020; Orth, 2021).

In contrast, the ENSO-related mode shows different CCM characteristics in the two directions (Fig. 4). The cross-map skill for $PWV_{ENSO} \rightarrow ENSO$ converges to $\rho = 0.91$ and is statistically significant ($p = 0.001$; Fig. 4c). By comparison, the $ENSO \rightarrow PWV_{ENSO}$ direction shows weaker convergence with $\rho = 0.73$ and does not pass the 95% significance threshold ($p = 0.900$; Fig. 4b). These results suggest that PWV_{ENSO} contains dynamical information related to ENSO evolution, whereas the reverse direction is not supported by the CCM significance test. This apparent asymmetry does not necessarily

https://doi.org/10.5194/egusphere-2026-3934
Preprint. Discussion started: 11 August 2026

contradict the expected influence of ENSO-related SST anomalies on atmospheric water vapour. Instead, it suggests that the inferred coupling may depend on the temporal offset between ENSO variability and the PWV response. This interpretation is consistent with the lead–lag analysis, which shows that ONI leads PWV_{ENSO} by approximately 12 months. Therefore, an extended CCM analysis is needed to examine whether ENSO exerts a delayed influence on the ENSO-related PWV component.

Extended CCM analyses were further performed over lags from -18 to $+18$ months to examine the lag dependence of the coupling. Fig. 5 shows the results for global warming and PWV_{GW}. Significant cross-map relationships are identified over a broad range of lags in both directions (Fig. 5a). The maximum cross-map skill for $GW \rightarrow PWV_{GW}$ occurs at $l = -8$ months, with $\rho = 0.831$ (Fig. 5b), and the corresponding surrogate test confirms statistical significance ($p = 0.001$; (Fig. 5d). In contrast, the $PWV_{GW} \rightarrow GW$ direction reaches its maximum cross-map skill at $l = 10$ months with $\rho = 0.642$ (Fig. 5c) and also passes the significance test ($p = 0.035$; Fig. 5e).

According to the extended CCM framework proposed by Ye et al. (2015), negative optimal lags are generally consistent with causal forcing from the driving variable to the response variable, whereas positive optimal lags are more commonly associated with generalized synchrony under strong unidirectional forcing. In this study, the strongest $GW \rightarrow PWV_{GW}$ relationship occurs at a negative lag, indicating that changes in global temperature tend to precede the adjustment of atmospheric water vapour. This result is physically consistent with the thermodynamic dependence of atmospheric water vapour on temperature. By comparison, the positive optimal lag in the reverse direction suggests that the apparent $PWV_{GW} \rightarrow GW$ relationship is more likely related to synchronization effects rather than an independent influence from atmospheric water vapour to global temperature. Overall, the extended CCM results support a dominant warming-to-PWV coupling, with PWV_{GW} primarily reflecting a delayed atmospheric-moisture response to global warming.

Fig. 6 presents the extended CCM results for ENSO and PWV_{ENSO}. The maximum cross-map skill for $ENSO \rightarrow PWV_{ENSO}$ occurs at $l = -11$ months, with $\rho = 0.901$ (Fig. 6b), and is statistically significant ($p = 0.046$; Fig. 6d). The $PWV_{ENSO} \rightarrow ENSO$ direction reaches its maximum at $l = -7$ months with $\rho = 0.949$ (Fig. 6c) and also passes the significance test ($p = 0.001$; Fig. 6e). The optimal lags in both directions are negative, consistent with bidirectional coupling within the extended CCM framework of Ye et al. (2015). Combined with the approximately 12-month lead of ONI relative to PWV_{ENSO} identified in the time-series analysis (Fig. 2d), these results further support that ENSO-related SST anomalies exert a delayed influence on large-scale atmospheric water vapour variability. Meanwhile, the significant negative lag in the $PWV_{ENSO} \rightarrow ENSO$ direction suggests that atmospheric water vapour variability may also contain feedback-related information on ENSO evolution. Overall, the extended CCM results suggest that the ENSO–PWV_{ENSO} interaction involves both the delayed response of atmospheric water vapour to ENSO forcing and a possible feedback effects from atmospheric water vapour to ENSO (Tian et al., 2026).

3.3 Causal Evolution Under Accelerated Warming

The BEAST analysis identifies a pronounced breakpoint in the global mean temperature series around October 2013 (Fig. 7a), separating the record into a slow-warming period (P1: January 2003–October 2013) and an accelerated-warming period (P2: November 2013–December 2025). The estimated warming rate increases markedly from 0.06 °C/decade during P1 to

https://doi.org/10.5194/egusphere-2026-3934
Preprint. Discussion started: 11 August 2026

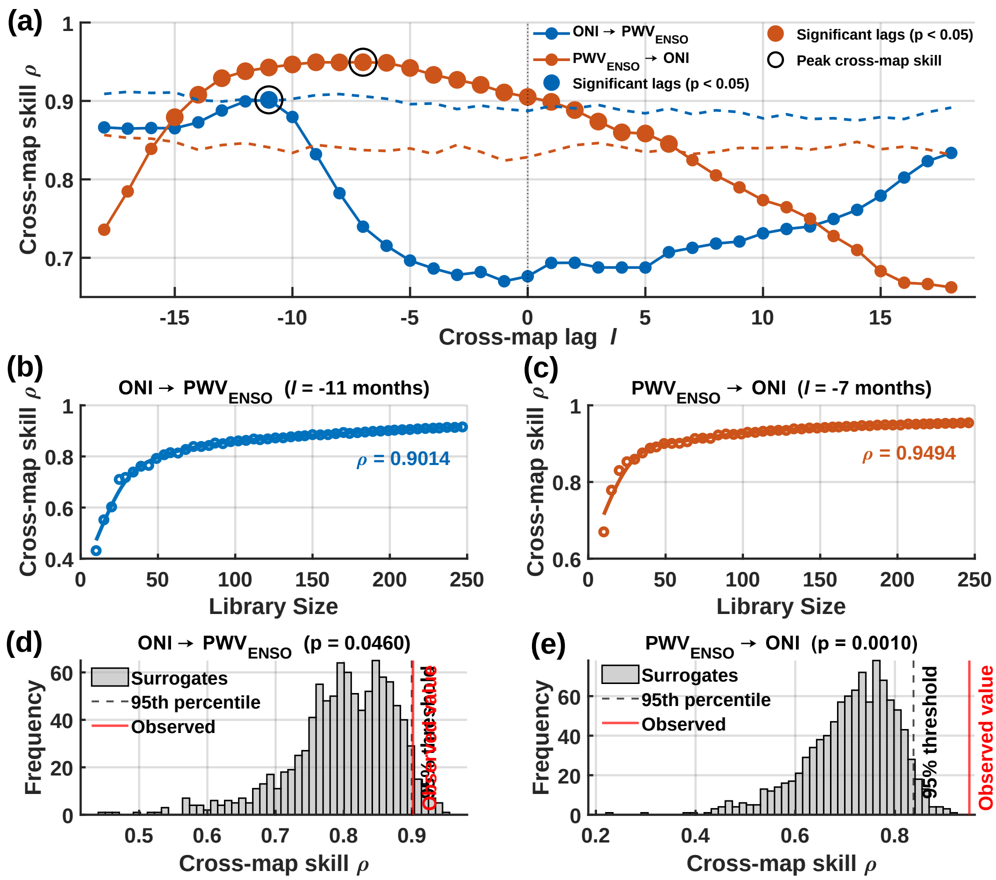

Figure 6. Extended CCM analysis between ENSO and PWV_{ENSO}. (a) Lag-dependent cross-map skill (ρ) for both directions over lags from -18 to $+18$ months. Large filled circles indicate lags passing the 95% surrogate significance test, black circles denote the optimal lag with maximum cross-map skill, and dashed lines represent the corresponding 95% surrogate thresholds. (b)–(c) Convergence of cross-map skill with increasing library size at the optimal lag for $ENSO \rightarrow PWV_{ENSO}$ and $PWV_{ENSO} \rightarrow ENSO$, respectively. (d)–(e) Phase-randomized surrogate significance tests at the optimal lag for each direction.

0.32 °C/decade during P2, indicating a substantial intensification of global warming after 2013. The breakpoint is used here to define two observational periods for subsequent comparison.

The corresponding PWV components exhibit distinct behaviors across the two warming regimes (Fig. 7b,c). During P1, both GW and PWV_{GW} display relatively weak variability and limited long-term change. In contrast, P2 is characterized by larger amplitudes and more coherent long-term variations in both series, consistent with the accelerated warming trend. By comparison, the oscillatory behavior of ONI and PWV_{ENSO} remains evident throughout both periods, indicating that ENSO-related variability persists under different warming backgrounds.

The relationship between GW and PWV_{GW} shows a clear dependence on the warming background. Over the full study period, the two variables exhibit their strongest correlation at near-zero lag ($r = 0.79$), indicating an approximately synchronous

https://doi.org/10.5194/egusphere-2026-3934
Preprint. Discussion started: 11 August 2026

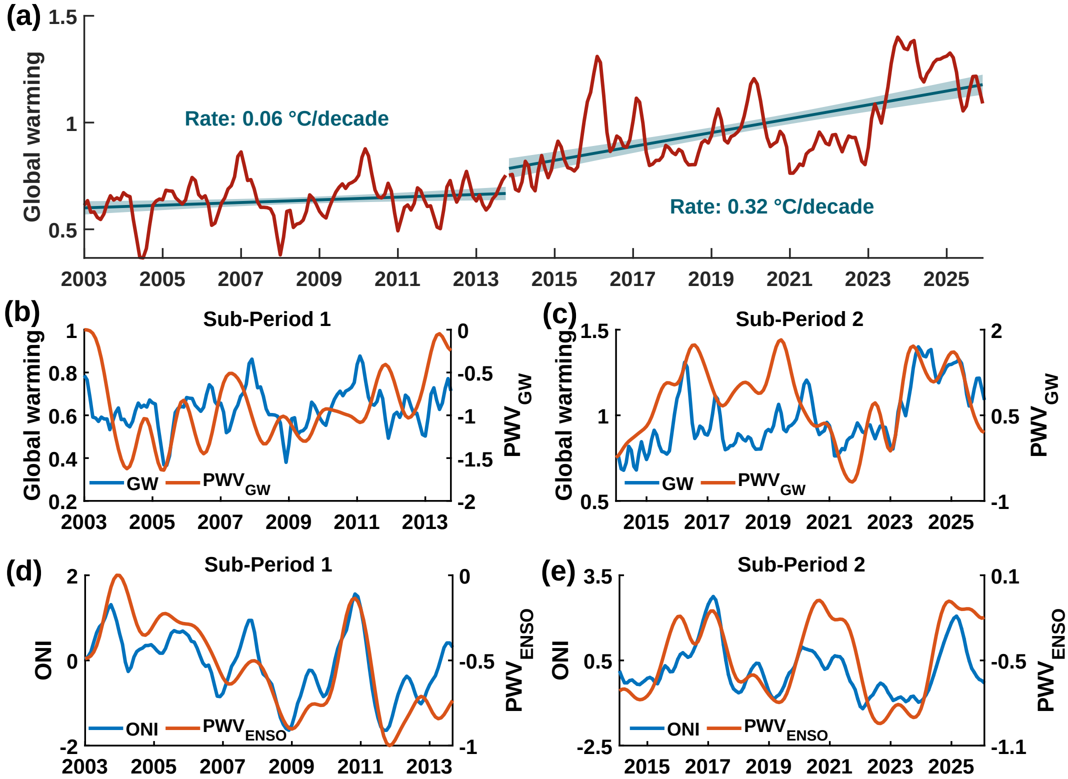

Figure 7. BEAST-based warming-stage segmentation and temporal evolution of climate indices and ICA-derived PWV components. (a) BEAST decomposition of global mean temperature, showing a major breakpoint in October 2013 separating slow-warming (P1) and accelerated-warming (P2) stages, with linear trends indicated by blue lines. (b)–(c) Temporal evolution of GW and PWV_{GW} during P1 and P2. (d)–(e) Temporal evolution of ONI and PWV_{ENSO} during P1 and P2.

relationship. However, during P1, the correlation weakens substantially and does not pass the significance test ($r = 0.21$), likely because the warming trend during this stage is relatively weak. During P2, the correlation strengthens and remains centered near zero lag ($r = 0.50$, $p < 0.05$). The stronger and statistically significant relationship during P2 indicates that the warming-related PWV component becomes more tightly linked to global temperature when the background warming is more rapid.

For the ENSO-related mode, the strongest lagged correlation consistently occurs when PWV_{ENSO} lags ONI by approximately 12 months (Fig. 7d,e). Over the full 2003–2025 period, the maximum lagged correlation reaches $r = 0.77$. Comparable lag structures are observed in both subperiods, with peak correlations of $r = 0.80$ during P1 and $r = 0.76$ during P2. The persistence of this approximately 12-month lag suggests that the delayed PWV response to ENSO-related SST variability remains temporally stable across the transition to accelerated warming.

To examine how the warming-related relationship changes under different warming backgrounds, the relationship between GW and PWV_{GW} is analysed separately for the two subperiods. Because the segmented GW and PWV_{GW} series are strongly trend-dominated and exhibit limited low-frequency variability after detrending, CCM analysis is not suitable for these

https://doi.org/10.5194/egusphere-2026-3934
Preprint. Discussion started: 11 August 2026

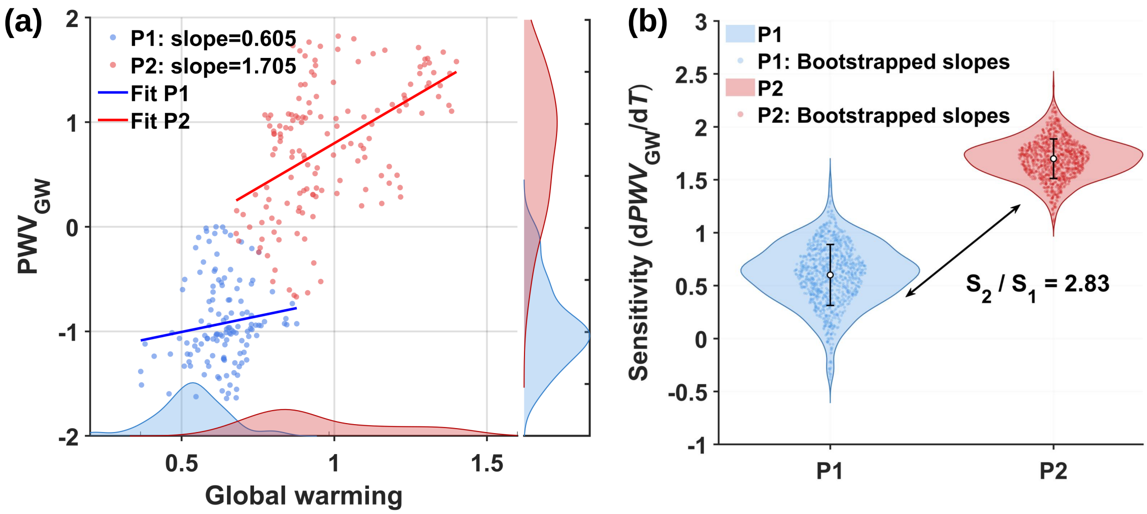

Figure 8. Enhanced sensitivity of atmospheric water vapour to global warming during the accelerated-warming stage. (a) Regression relationship between GW and PWV_{GW} for the two subperiods. (b) Bootstrap distributions of the regression slopes for P1 and P2.

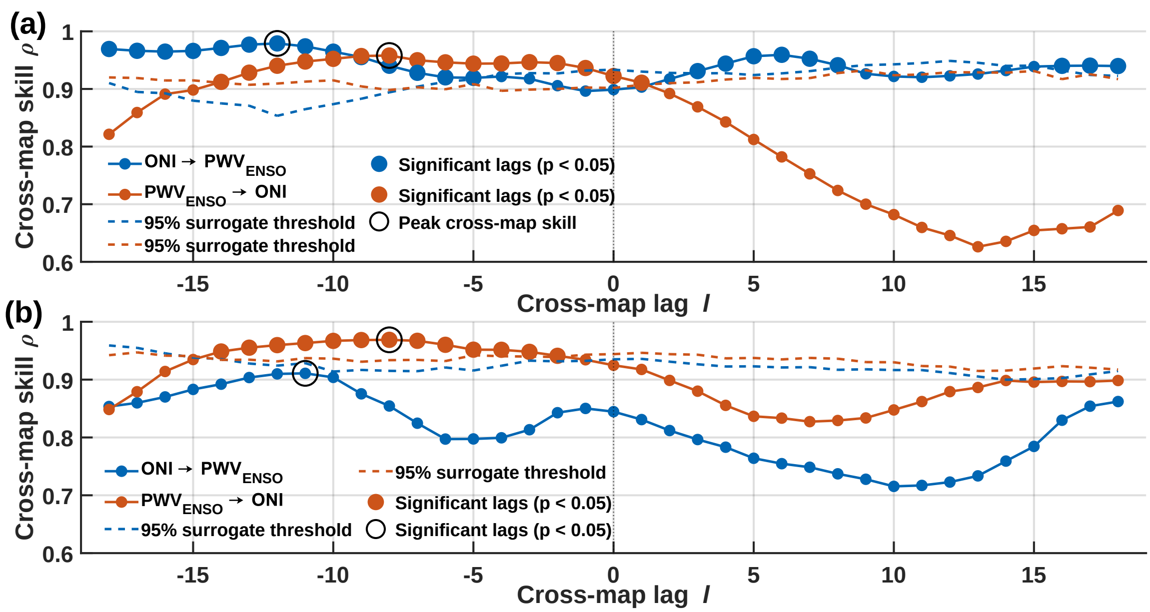

Figure 9. Extended CCM results for the ENSO–PWV_{ENSO} coupling during the two warming stages. (a) Lag-dependent cross-map skill for P1. (b) Lag-dependent cross-map skill for P2. Large filled circles indicate lags passing the 95% significance test, black circles denote the optimal lag corresponding to the maximum cross-map skill, and dashed lines represent the corresponding 95% surrogate significance thresholds for each direction.

https://doi.org/10.5194/egusphere-2026-3934
Preprint. Discussion started: 11 August 2026

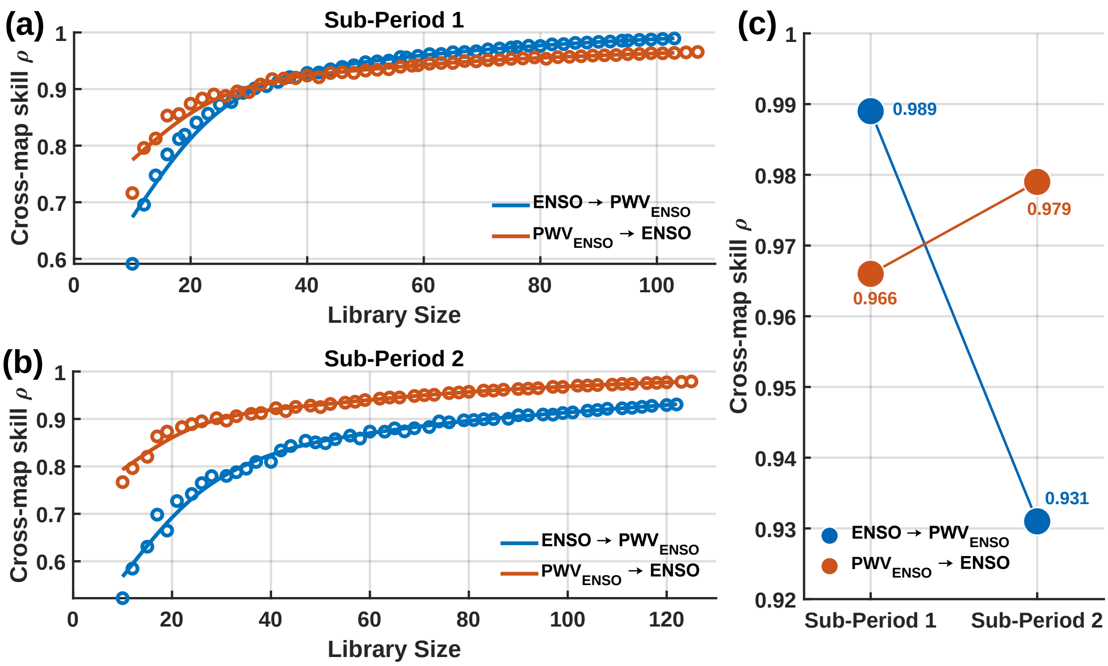

Figure 10. Convergence characteristics of the extended CCM analyses for the ENSO–PWV_{ENSO} coupling under different warming stages. (a)–(b) Convergence of cross-map skill with increasing library size at the optimal lag during P1 and P2, respectively. (c) Comparison of the maximum cross-map skill between the two subperiods for both causal directions.

subperiod records. Therefore, linear regression is used to quantify the sensitivity of the warming-related PWV component to temperature change during P1 and P2.

Fig. 8 shows the regression relationships between GW and PWV_{GW} for the two subperiods. The regression slope increases substantially from 0.61 during P1 to 1.71 during P2 (Fig. 8a), indicating a pronounced enhancement in the sensitivity of PWV_{GW} to warming during the accelerated-warming stage. Bootstrap resampling with 1,000 iterations further confirms the robustness of this change. The slope distributions for P1 and P2 exhibit only minimal overlap (Fig. 8b), and a two-sample Z-test indicates that the difference between the mean slopes is highly significant ($p < 0.0001$). The ratio between the two mean slopes reaches approximately 2.83.

The enhanced sensitivity during P2 suggests that atmospheric water vapour responds more strongly to warming under a warmer climate background. This behavior is consistent with the Clausius–Clapeyron relationship, under which a warmer atmosphere can retain more water vapour for a given temperature increase. As a result, accelerated warming is accompanied not only by a faster rise in global temperature, but also by an enhanced sensitivity of atmospheric water vapour to temperature change.

The evolution of the ENSO–PWV_{ENSO} coupling under different warming backgrounds is further examined using the extended CCM for P1 and P2 separately (Fig. 9). In both subperiods, the optimal cross-map lags remain negative in the

https://doi.org/10.5194/egusphere-2026-3934
Preprint. Discussion started: 11 August 2026

two directions, consistent with bidirectional coupling according to the extended CCM framework of Ye et al. (2015). During P1, the maximum cross-map skill for $ENSO \rightarrow PWV_{ENSO}$ occurs at $l = -12$ months, whereas the optimal lag for $PWV_{ENSO} \rightarrow ENSO$ is $l = -8$ months (Fig. 9a). Both directions pass the significance test based on phase-randomized surrogates. During P2, the optimal lag structure remains nearly unchanged, with peak cross-map skills occurring at $l = -11$ months for $ENSO \rightarrow PWV_{ENSO}$ and $l = -8$ months for $PWV_{ENSO} \rightarrow ENSO$ (Fig. 9b). The persistence of similar negative optimal lags across the two warming stages indicates that the lag-dependent ENSO–PWV interaction is largely preserved under accelerated warming.

Fig. 10 shows the convergence behavior at the optimal lags. During P1, both directions exhibit clear convergence with increasing library size, and the maximum cross-map skills reach $\rho = 0.989$ for $ENSO \rightarrow PWV_{ENSO}$ and $\rho = 0.966$ for $PWV_{ENSO} \rightarrow ENSO$ (Fig. 10a,c). During P2, the maximum cross-map skill for $PWV_{ENSO} \rightarrow ENSO$ increases slightly to $\rho = 0.979$, suggesting a modest strengthening of the atmospheric water vapour feedback to ENSO (Fig. 10b,c). In contrast, the cross-map skill for $ENSO \rightarrow PWV_{ENSO}$ decreases to $\rho = 0.931$. Although the observed cross-map skill remains close to the 95% surrogate significance threshold, the convergence curve still increases steadily with library size, suggesting that the ENSO influence on atmospheric water vapour remains detectable during the accelerated-warming stage.

Overall, the segmented extended CCM analyses suggest that the bidirectional coupling structure between ENSO and atmospheric water vapour persists across different warming backgrounds, although the relative strength of the two directions changes during the accelerated-warming period. In particular, the $ENSO \rightarrow PWV_{ENSO}$ pathway weakens during P2, whereas the $PWV_{ENSO} \rightarrow ENSO$ pathway remains comparatively robust. These results suggest that accelerated warming may alter the relative balance of the ENSO–atmospheric water-vapour coupling while preserving its overall lag-dependent interaction pattern.

4 Discussion

This study shows that global GNSS-derived PWV contains separable water vapour signals associated with sustained global warming and ENSO-related interannual variability. The ICA results indicate that these two signals differ not only in their temporal behavior, but also in their spatial expression and coupling structure. This separation is important because atmospheric water vapour is affected simultaneously by long-term thermodynamic moistening, ocean–atmosphere variability, and regional moisture transport. The results therefore suggest that long-term GNSS PWV observations provide independent ground-based evidence for how atmospheric moisture responds to both forced warming and natural climate variability.

The warming-related component has the clearest physical interpretation. Its near-synchronous relationship with global mean temperature, predominantly positive spatial loading pattern, and dominant $GW \rightarrow PWV_{GW}$ coupling all indicate that this component mainly represents the thermodynamic moistening of the atmosphere under global warming. The stronger regression slope during the accelerated-warming period further suggests that the PWV response to temperature becomes more pronounced under a warmer background climate. This behaviour is consistent with Clausius–Clapeyron thermodynamic scaling, under

https://doi.org/10.5194/egusphere-2026-3934
Preprint. Discussion started: 11 August 2026

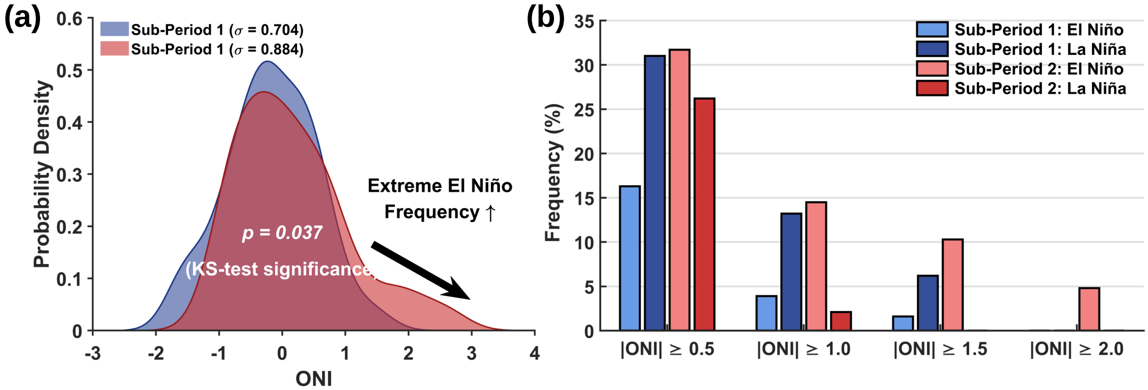

Figure 11. ENSO variability under different warming stages. (a) Probability density distributions of ONI during P1 and P2. (b) Frequencies of El Niño and La Niña events under different ONI intensity thresholds for the two subperiods.

which a warmer atmosphere can hold more water vapour for a given temperature increase. Thus, accelerated warming appears to strengthen the thermodynamic control of temperature on global land atmospheric moisture.

The ENSO-related component exhibits a more complex, lag-dependent coupling structure. The approximately 12-month lead of ONI relative to PWV_{ENSO}, together with the extended CCM results, supports a delayed influence of ENSO-related SST variability on large-scale atmospheric water vapour. At the same time, the significant $PWV_{ENSO} \rightarrow ENSO$ pathway suggests that water-vapour variability may contain feedback-related information on ENSO evolution or reflect shared coupled ocean–atmosphere dynamics. This suggests that the ENSO-related PWV signal reflects not only a delayed atmospheric response to ENSO forcing, but also a broader lag-dependent coupling with ENSO-related ocean–atmosphere variability.

A key implication of the segmented analysis is that accelerated warming changes the relative balance between thermodynamic moistening and ENSO-related variability in the PWV field. Although the lag structure of the ENSO–PWV_{ENSO} relationship remains broadly stable across the two warming periods, the $ENSO \rightarrow PWV_{ENSO}$ cross-map skill weakens during the accelerated-warming stage. This weakening is unlikely to result from reduced ENSO activity, because ONI variability remains strong during P2: the ONI standard deviation increases from 0.704 in P1 to 0.884 in P2, the frequency of strong and extreme El Niño events also increases, and the ONI distributions differ significantly between the two periods according to the Kolmogorov–Smirnov test ($p = 0.037$; Fig. 11). A more plausible explanation is that the strengthened warming-related moistening signal increases the thermodynamic contribution to PWV variability, thereby reducing the relative imprint of ENSO-driven variability in the global land PWV field. In this sense, accelerated warming may alter the behavior of atmospheric water vapour by increasing the dominance of long-term thermodynamic forcing over interannual dynamical variability.

Several limitations should be noted. The GNSS PWV record spans slightly more than two decades, which limits the robustness of nonlinear coupling analysis, especially after segmentation into two warming periods. In addition, the heterogeneous land-based distribution of GNSS stations means that the results mainly represent GNSS-observed land PWV rather than the

https://doi.org/10.5194/egusphere-2026-3934
Preprint. Discussion started: 11 August 2026

full global water-vapour field. Finally, although ICA and CCM provide useful diagnostics for separating climate-related PWV signals and assessing directional coupling, residual signal mixing and uncertainties in causal interpretation may remain.

Despite these limitations, the results demonstrate that global GNSS PWV observations provide physically meaningful evidence for changes in the state and behaviour of atmospheric moisture under sustained warming and ENSO-related variability. The findings suggest that accelerated warming strengthens the thermodynamic control on atmospheric water vapour while reducing the relative dominance of ENSO-related variability in the global land PWV field. This indicates that the atmospheric water-vapour response to climate forcing and interannual variability is not stationary, but evolves as the background climate becomes warmer.

5 Conclusions

This study investigated the coupling between global GNSS-derived PWV and large-scale climate variability over 2003–2025 by combining ICA, CCM, extended CCM, and BEAST-based warming-stage detection. Two climate-related PWV components were identified: a warming-related component (PWV_{GW}) and an ENSO-related component (PWV_{ENSO}).

The results show that sustained warming and ENSO-related variability leave separable signals in the GNSS-observed land PWV field. PWV_{GW} exhibits a coherent long-term increase and is closely linked to global mean temperature, with a peak correlation of $r = 0.79$ at zero lag. In contrast, PWV_{ENSO} is dominated by interannual variability and lags ONI by approximately 12 months, with a peak correlation of $r = 0.77$. These findings indicate that long-term GNSS PWV observations provide independent ground-based evidence for distinct warming-driven and ENSO-related water-vapour variability. Previous GNSS-based PWV studies have mainly examined regional PWV variability, long-term trends, or ENSO-related correlations using covariance-based methods such as EOF/PCA. By using ICA to better account for the non-Gaussian nature of ENSO-related variability, this study may provide the first global-scale, robust separation of both warming-related and ENSO-related PWV signals from long-term GNSS observations.

The coupling analyses show that PWV_{GW} responds primarily to global warming, consistent with the thermodynamic dependence of atmospheric moisture on temperature. By contrast, PWV_{ENSO} exhibits lag-dependent bidirectional coupling, indicating a delayed atmospheric water-vapour response to ENSO-related SST variability and a possible feedback link between atmospheric moisture and ENSO evolution. This advances previous correlation-based interpretations by showing that the ENSO–PWV relationship is not only statistically associated, but also strongly lag-dependent and directionally asymmetric.

After the transition to accelerated warming around 2013, the sensitivity of PWV_{GW} to temperature increases substantially, with the regression slope rising from 0.61 during P1 to 1.71 during P2. Meanwhile, the $ENSO \rightarrow PWV_{ENSO}$ cross-map skill weakens during P2 despite sustained ENSO variability, with the ONI standard deviation increasing from 0.704 to 0.884. These findings suggest that accelerated warming strengthens the thermodynamic contribution to atmospheric water vapour and reduces the relative dominance of ENSO-related variability in the global land PWV field. This provides new observational evidence that the relative influence of forced warming and interannual ENSO variability on atmospheric moisture can shift as the background climate warms.

https://doi.org/10.5194/egusphere-2026-3934
Preprint. Discussion started: 11 August 2026

Several limitations should be acknowledged. The GNSS record is still relatively short for segmented nonlinear coupling analysis, and the station network mainly represents land areas with heterogeneous spatial coverage. These factors may introduce some uncertainty in the estimated coupling strength, but they do not change the overall consistency among the ICA, lead–lag, CCM, and physical interpretation results. In addition, ICA and CCM provide diagnostic evidence for signal separation and directional coupling, although residual signal mixing and uncertainties in causal interpretation may remain. Future work using longer GNSS records and improved station coverage would help extend this framework and further clarify how atmospheric moisture behaviour evolves under continued warming.

Overall, this study provides observational evidence that the atmospheric water-vapour response to sustained warming and ENSO-related interannual variability is not stationary but evolves as the background climate warms. The results imply that atmospheric moisture is becoming increasingly shaped by warming-driven thermodynamic control, with important implications for understanding the changing state and behaviour of atmospheric moisture and the future evolution of the atmospheric branch of the global water cycle.

Data availability. All data used in this paper are freely available. The GNSS precipitable water vapour (PWV) records for January 2003 to December 2021 are available from PANGAEA, the Data Publisher for Earth & Environmental Science, at https://doi.pangaea.de/10.1594/PANGAEA.982476 Wang et al. (2025). PWV data from January 2022 to December 2025 are downloaded from the University of Nevada, Reno (UNR) Geodesy Laboratory at https://geodesy.unr.edu/gps_timeseries/IGS20/trop/. Global mean surface temperature (GMST) series are from the NASA Goddard Institute for Space Studies (GISS) at https://data.giss.nasa.gov/gistemp/. The Oceanic Niño Index (ONI) is provided by the NOAA Climate Prediction Center (CPC) at https://www.cpc.ncep.noaa.gov/data/indices/.

Author contributions. YG and WZ designed the study and developed the main research framework. YG performed the data processing, analysis, visualization, and manuscript drafting. SZ and ZC contributed to GNSS PWV data preparation, quality control, and result validation. CL and LL assisted with methodological implementation, statistical analysis, and interpretation of the results. WZ supervised the research, provided guidance on the scientific interpretation, and revised the manuscript critically. All authors discussed the results, reviewed the manuscript, and approved the final version.

Competing interests. The contact author has declared that none of the authors has any competing interests.

Disclaimer. Publisher's note: Copernicus Publications remains neutral with regard to jurisdictional claims made in the text, published maps, institutional affiliations, or any other geographical representation in this paper.

https://doi.org/10.5194/egusphere-2026-3934
Preprint. Discussion started: 11 August 2026

445 *Acknowledgements.* The authors acknowledge the thoughtful comments and suggestions of the two anonymous referees.

Financial support. This study was supported by grants from the National Natural Science Foundation of China (42271460,42404016,42374040), the Natural Science Foundation of Jiangsu Province (BK20241669), and the Outstanding Youth Foundation Project of Jiangxi Provincial Natural Science Foundation (20242BAB22001).

https://doi.org/10.5194/egusphere-2026-3934
Preprint. Discussion started: 11 August 2026

References

Aires, F., Chédin, A., and Nadal, J.-P.: Independent component analysis of multivariate time series: Application to the tropical SST variability, Journal of Geophysical Research: Atmospheres, 105, 17 437–17 455, https://doi.org/10.1029/2000JD900152, 2000.

Ali, H., Peleg, N., and Fowler, H. J.: Global Scaling of Rainfall With Dewpoint Temperature Reveals Considerable Ocean-Land Difference, Geophysical Research Letters, 48, e2021GL093 798, https://doi.org/10.1029/2021GL093798, 2021.

Baldysz, Z., Nykiel, G., Latos, B., Baranowski, D. B., and Figurski, M.: Interannual Variability of the GNSS Precipitable Water Vapor in the Global Tropics, Atmosphere, 12, https://doi.org/10.3390/atmos12121698, 2021.

Ban, J., Ni, S., Han, F., He, B., and Wang, W.: Uncovering nonlinear causal relationships and propagation dynamics of drought types in Xinjiang using convergent cross mapping, Journal of Environmental Management, 393, 127 165, https://doi.org/10.1016/j.jenvman.2025.127165, 2025.

Basili, P., Bonafoni, S., Ferrara, R., Ciotti, P., Fionda, E., and Arnbrosini, R.: Atmospheric water vapor retrieval by means of both a GPS network and a microwave radiometer during an experimental campaign in Cagliari, Italy, in 1999, IEEE Transactions on Geoscience and Remote Sensing, 39, 2436–2443, https://doi.org/10.1109/36.964980, 2001.

Bevacqua, E., Rakovec, O., Schumacher, D., Kumar, R., Thober, S., Samaniego, L., Seneviratne, S., and Zscheischler, J.: Direct and lagged climate change effects intensified the 2022 European drought, Nature Geoscience, 17, 1100–1107, https://doi.org/10.1038/s41561-024-01559-2, 2024.

Bevis, M., Businger, S., Herring, T. A., Rocken, C., Anthes, R. A., and Ware, R. H.: GPS meteorology: Remote sensing of atmospheric water vapor using the global positioning system, Journal of Geophysical Research: Atmospheres, 97, 15 787–15 801, https://doi.org/10.1029/92JD01517, 1992.

Bevis, M., Businger, S., Chiswell, S., Herring, T. A., Anthes, R. A., Rocken, C., and Ware, R. H.: GPS Meteorology: Mapping Zenith Wet Delays onto Precipitable Water, Journal of Applied Meteorology and Climatology, 33, 379 – 386, https://doi.org/10.1175/1520-0450(1994)033<0379:GMMZWD>2.0.CO;2, 1994.

Bingham, E. and Hyvärinen, A.: A Fast Fixed-Point Algorithm for Independent Component Analysis of Complex Valued Signals, International Journal of Neural Systems, 10, 1–8, https://doi.org/10.1142/S0129065700000028, 2000.

Bonotto, G., Peterson, T., Fowler, K., and Western, A.: Identifying Causal Interactions Between Groundwater and Streamflow Using Convergent Cross-Mapping, Water Resources Research, 58, https://doi.org/10.1029/2021WR030231, 2022.

Chen, Z., Li, J., Luo, J., and Cao, X.: A New Strategy for Extracting ENSO Related Signals in the Troposphere and Lower Stratosphere from GNSS RO Specific Humidity Observations, Remote Sensing, 10, 503, https://doi.org/10.3390/rs10040503, 2018.

Chen, Z., Li, L., Wang, B., Fan, J., Lu, T., and Lv, K.: The impact of global warming on ENSO from the perspective of objective signals, Atmospheric Research, 299, 107 176, https://doi.org/10.1016/j.atmosres.2023.107176, 2024.

Comon, P.: Independent component analysis, A new concept?, Signal Processing, 36, 287–314, https://doi.org/10.1016/0165-1684(94)90029-9, 1994.

Curtis, S.: The El Niño–Southern Oscillation and Global Precipitation, Geography Compass, 2, 600–619, https://doi.org/10.1111/j.1749-8198.2008.00105.x, 2008.

Diaz, H. F., Hoerling, M. P., and Eischeid, J. K.: ENSO variability, teleconnections and climate change, International Journal of Climatology, 21, 1845–1862, https://doi.org/10.1002/joc.631, 2001.

https://doi.org/10.5194/egusphere-2026-3934
Preprint. Discussion started: 11 August 2026

Ding, Q. and Fu, Q.: A warming tropical central Pacific dries the lower stratosphere, Climate dynamics, 50, 2813–2827, https://doi.org/10.1007/s00382-017-3774-y, 2018.

Ebisuzaki, W.: A Method to Estimate the Statistical Significance of a Correlation When the Data Are Serially Correlated, Journal of Climate, 10, 2147 – 2153, https://doi.org/10.1175/1520-0442(1997)010<2147:AMTETS>2.0.CO;2, 1997.

Edström, F. and Dahlbäck, P.: Atmospheric water vapour as a potential water source and its impact on energy systems, Nature Reviews Materials, 9, 671–672, https://doi.org/10.1038/s41578-024-00727-5, 2024.

Fischer, E., Bador, M., Huser, R., Kendon, E., Robinson, A., and Sippel, S.: Record-breaking extremes in a warming climate, Nature Reviews Earth & Environment, 6, https://doi.org/10.1038/s43017-025-00681-y, 2025.

Foster, G. and Rahmstorf, S.: Global Warming Has Accelerated Significantly, Geophysical Research Letters, 53, e2025GL118 804, https://doi.org/10.1029/2025GL118804, 2026.

Fraser, A. M. and Swinney, H. L.: Independent coordinates for strange attractors from mutual information, Phys. Rev. A, 33, 1134–1140, https://doi.org/10.1103/PhysRevA.33.1134, 1986.

Gebrechorkos, S., Sheffield, J., Vicente-Serrano, S., Funk, C., Miralles, D., Peng, J., Dyer, E., Talib, J., Beck, H., Singer, M., and Dadson, S.: Warming accelerates global drought severity, Nature, 642, 628–635, https://doi.org/10.1038/s41586-025-09047-2, 2025.

He, Q., Shen, Z., Wan, M., and Li, L.: Precipitable Water Vapor Converted from GNSS-ZTD and ERA5 Datasets for the Monitoring of Tropical Cyclones, IEEE Access, 8, 87 275–87 290, https://doi.org/10.1109/ACCESS.2020.2991094, 2020.

Hyvärinen, A. and Oja, E.: Independent component analysis: algorithms and applications, Neural Networks, 13, 411–430, https://doi.org/10.1016/S0893-6080(00)00026-5, 2000.

Jin, S., Li, Z., and Cho, J.: Integrated Water Vapor Field and Multiscale Variations over China from GPS Measurements, Journal of Applied Meteorology and Climatology, 47, 3008 – 3015, https://doi.org/10.1175/2008JAMC1920.1, 2008.

Jutten, C. and Herault, J.: Blind separation of sources, part I: An adaptive algorithm based on neuromimetic architecture, Signal Processing, 24, 1–10, https://doi.org/10.1016/0165-1684(91)90079-X, 1991.

Kelsey, V., Riley, S., and Minschwaner, K.: Atmospheric precipitable water vapor and its correlation with clear-sky infrared temperature observations, Atmospheric Measurement Techniques, 15, 1563–1576, https://doi.org/10.5194/amt-15-1563-2022, 2022.

Kennel, M. B., Brown, R., and Abarbanel, H. D. I.: Determining embedding dimension for phase-space reconstruction using a geometrical construction, Physical Review A, 45, 3403–3411, https://doi.org/10.1103/PhysRevA.45.3403, 1992.

Lenssen, N., Schmidt, G. A., Hendrickson, M., Jacobs, P., Menne, M. J., and Ruedy, R.: A NASA GISTEMPv4 Observational Uncertainty Ensemble, Journal of Geophysical Research: Atmospheres, 129, e2023JD040 179, https://doi.org/10.1029/2023JD040179, 2024.

Li, X., Wang, C., and Lan, J.: Role of the South China Sea in Southern China rainfall: meridional moisture flux transport, Climate Dynamics, 56, 2551–2568, https://doi.org/10.1007/s00382-020-05603-w, 2021.

Lu, J., Xie, F., Sun, C., Luo, J., Cai, Q., Zhang, J., Li, J., and Tian, H.: Analysis of factors influencing tropical lower stratospheric water vapor during 1980–2017, npj Climate and Atmospheric Science, 3, 35, https://doi.org/10.1038/s41612-020-00138-7, 2020.

Martínková, M. and Kyselý, J.: Overview of Observed Clausius-Clapeyron Scaling of Extreme Precipitation in Midlatitudes, Atmosphere, 11, 786–786, https://doi.org/10.3390/atmos11080786, 2020.

Nayak, S. and Takemi, T.: Regional and vertical scaling of water vapor with temperature over Japan during extreme precipitation in a changing climate, Scientific Reports, 15, 34 826–34 826, https://doi.org/10.1038/s41598-025-22287-6, 2025.

Nilsson, T. and Elgered, G.: Long-term trends in the atmospheric water vapor content estimated from ground-based GPS data, Journal of Geophysical Research: Atmospheres, 113, https://doi.org/10.1029/2008JD010110, 2008.

Orth, R.: When the Land Surface Shifts Gears, AGU Advances, 2, e2021AV000 414, https://doi.org/10.1029/2021AV000414, 2021.

Patel, V. and Kuttippurath, J.: Increase in Tropospheric Water Vapor Amplifies Global Warming and Climate Change, Ocean-Land-Atmosphere Research, 2, https://doi.org/10.34133/olar.0015, 2023.

Rocken, C., Ware, R., Van Hove, T., Solheim, F., Alber, C., Johnson, J., Bevis, M., and Businger, S.: Sensing atmospheric water vapor with the global positioning system, Geophysical Research Letters, 20, 2631–2634, https://doi.org/10.1029/93GL02935, 1993.

Rocken, C., Hove, T. V., Johnson, J., Solheim, F., Ware, R., Bevis, M., Chiswell, S., and Businger, S.: GPS/STORM—GPS Sensing of Atmospheric Water Vapor for Meteorology, Journal of Atmospheric and Oceanic Technology, 12, 468 – 478, https://doi.org/10.1175/1520-0426(1995)012<0468:GSOAWV>2.0.CO;2, 1995.

Schneider, E. K., Kirtman, B. P., and Lindzen, R. S.: Tropospheric Water Vapor and Climate Sensitivity, Journal of the Atmospheric Sciences, 56, 1649 – 1658, https://doi.org/10.1175/1520-0469(1999)056<1649:TWVACS>2.0.CO;2, 1999.

Sherwood, S. C., Roca, R., Weckwerth, T. M., and Andronova, N. G.: Tropospheric water vapor, convection, and climate, Reviews of Geophysics, 48, https://doi.org/10.1029/2009RG000301, 2010.

Shu, Z., Jin, J., Zhang, J., Wang, G., Lian, Y., Liu, Y., Bao, Z., Guan, T., He, R., Liu, C., and Jing, P.: 1.5°C and 2.0°C of global warming intensifies the hydrological extremes in China, Journal of Hydrology, 635, 131 229, https://doi.org/10.1016/j.jhydrol.2024.131229, 2024.

Sugihara, G., May, R., Ye, H., hao Hsieh, C., Deyle, E., Fogarty, M., and Munch, S.: Detecting Causality in Complex Ecosystems, Science, 338, 496–500, https://doi.org/10.1126/science.1227079, 2012.

Sun, L. and Lan, Y.: Statistical downscaling of daily temperature and precipitation over China using deep learning neural models: Localization and comparison with other methods, International Journal of Climatology, 41, 1128–1147, https://doi.org/10.1002/joc.6769, 2021.

Takens, F.: Detecting strange attractors in turbulence, in: Dynamical Systems and Turbulence, Warwick 1980, edited by Rand, D. and Young, L.-S., pp. 366–381, Springer Berlin Heidelberg, Berlin, Heidelberg, ISBN 978-3-540-38945-3, https://doi.org/10.1007/BFb0091924, 1981.

Theiler, J., Eubank, S., Longtin, A., Galdrikian, B., and Doyne Farmer, J.: Testing for nonlinearity in time series: the method of surrogate data, Physica D: Nonlinear Phenomena, 58, 77–94, https://doi.org/10.1016/0167-2789(92)90102-S, 1992.

Tian, F., Zhang, R., Liu, C., and Guan, C.: Rainfall sustains multiyear La Niña, Nature Communications, 17, https://doi.org/10.1038/s41467-026-68451-y, 2026.

Tregoning, P., Boers, R., O'Brien, D., and Hendy, M.: Accuracy of absolute precipitable water vapor estimates from GPS observations, Journal of Geophysical Research: Atmospheres, 103, 28 701–28 710, https://doi.org/10.1029/98JD02516, 1998.

Wang, D., Qin, Y., Xianjun, X., Zhang, Z., and Wu, X.: El Niño and El Niño Modoki variability based on a new ocean reanalysis, Ocean Dynamics, 62, https://doi.org/10.1007/s10236-012-0566-0, 2012.

Wang, R. and Ren, D.: Study on the nonlinear trend of water vapor and its response to ENSO events in Mainland China, in: Sixth International Conference on Geoscience and Remote Sensing Mapping (GRSM 2024), edited by Qin, Z., Chen, J., and Wu, H., vol. 13506, p. 135061R, International Society for Optics and Photonics, SPIE, https://doi.org/10.1117/12.3057524, 2025.

Wang, X., Zhang, K., Wu, S., Li, Z., Cheng, Y., Li, L., and Yuan, H.: The correlation between GNSS-derived precipitable water vapor and sea surface temperature and its responses to El Niño–Southern Oscillation, Remote Sensing of Environment, 216, 1–12, https://doi.org/10.1016/j.rse.2018.06.029, 2018.

Wang, X., Li, H., Choy, S., Huang, Q., Cai, W., Rea, A., Zhang, H., Elneser, L., and Kuleshov, Y.: A global GNSS climate data record from 5085 stations spanning up to 22 years, Earth System Science Data, 17, 5951–5982, https://doi.org/10.5194/essd-17-5951-2025, 2025.

https://doi.org/10.5194/egusphere-2026-3934
Preprint. Discussion started: 11 August 2026

Yang, B. and Tan, Z.-M.: Interactive Radiation Accelerates the Intensification of the Midlevel Vortex for Tropical Cyclogenesis, Journal of the Atmospheric Sciences, 77, 4051–4065, https://doi.org/10.1175/JAS-D-20-0094.1, 2020.

Ye, H., Deyle, E., Gilarranz, L., and Sugihara, G.: Distinguishing time-delayed causal interactions using convergent cross mapping, Scientific Reports, 5, 14 750, https://doi.org/10.1038/srep14750, 2015.

Yi, S. and Sneeuw, N.: Filling the Data Gaps Within GRACE Missions Using Singular Spectrum Analysis, Journal of Geophysical Research: Solid Earth, 126, e2020JB021 227, https://doi.org/10.1029/2020JB021227, 2021.

Yuan, L. L., Anthes, R. A., Ware, R. H., Rocken, C., Bonner, W. D., Bevis, M. G., and Businger, S.: Sensing climate change using the global positioning system, Journal of Geophysical Research: Atmospheres, 98, 14 925–14 937, https://doi.org/10.1029/93JD00948, 1993.

Zhang, K., Manning, T., Wu, S., Rohm, W., Silcock, D., and Choy, S.: Capturing the Signature of Severe Weather Events in Australia Using GPS Measurements, IEEE Journal of Selected Topics in Applied Earth Observations and Remote Sensing, 8, 1839–1847, https://doi.org/10.1109/JSTARS.2015.2406313, 2015.

Zhang, W., Gou, J., Möller, G., Zhang, S., Gao, Y., Wang, N., and Soja, B.: A New Deep-Learning-Assisted Global Water Vapor Stratification Model for GNSS Meteorology: Validations and Applications, IEEE Transactions on Geoscience and Remote Sensing, 62, 1–14, https://doi.org/10.1109/TGRS.2024.3479778, 2024.

Zhao, K., Wulder, M. A., Hu, T., Bright, R., Wu, Q., Qin, H., Li, Y., Toman, E., Mallick, B., Zhang, X., and Brown, M.: Detecting changepoint, trend, and seasonality in satellite time series data to track abrupt changes and nonlinear dynamics: A Bayesian ensemble algorithm, Remote Sensing of Environment, 232, 111 181, https://doi.org/10.1016/j.rse.2019.04.034, 2019.

Zhao, Q., Liu, Y., Yao, W., Ma, X., and Yao, Y.: A Novel ENSO Monitoring Method using Precipitable Water Vapor and Temperature in Southeast China, Remote Sensing, 12, https://doi.org/10.3390/rs12040649, 2020.